Defect-induced circulating thermal current in graphene with nanosized width

Masahiro Morooka,[1] Takahiro Yamamoto,[1,2] and Kazuyuki Watanabe[1,2]
[1]*Department of Physics, Tokyo University of Science, 1-3 Kagurazaka, Shinjuku-ku, Tokyo 162-8601, Japan*
[2]*CREST, Japan Science and Technology Agency, 4-1-8 Honcho Kawaguchi, Saitama 332-0012, Japan*
(Received 2 October 2007; revised manuscript received 28 November 2007; published 22 January 2008)

A unique thermal transport mechanism has been predicted in graphene nanoribbons with Stone-Wales defects via two complementary approaches: the nonequilibrium Green's function method and the phonon-wave packet scattering method. In the low-energy region, the thermal current is carried by phonons with wavelength longer than the defect size, which flows ballistically along the edges of the ribbons. In contrast, high-energy phonons, with short wavelengths, are strongly scattered. The phonon transmission is reduced to zero for a specific phonon energy and a noticeable circulating thermal current is observed in the heptagonal rings of the Stone-Wales defect around the zero-transmission point.

DOI: 10.1103/PhysRevB.77.033412 PACS number(s): 63.22.−m, 63.20.kp, 44.10.+i

I. INTRODUCTION

A graphene nanoribbon (GNR) is a type of quasi-one-dimensional carbon material with nanosized width that is obtained by cutting a single-walled carbon nanotube along its axis.[1] Owing to their open structure with edges, GNRs have several unique properties. In particular, zigzag GNRs (ZGNRs) exhibit *edge states*, close to the Fermi level, for which the electrons are highly localized on the edge carbon atoms.[2] Considering the potentially important influence of these edges states, the electronic transport properties of GNRs have been studied extensively.[3–5]

In addition to electronic transport, knowledge of thermal transport properties of GNRs is also critical for designing reliable GNR-based electronic and thermal devices. However, thermal transport in GNRs has not received significant attention thus far.[6] The first objective of this study therefore was to clarify whether GNRs show remarkable thermal transport properties and whether these properties depend on the edges as well. The second objective was to assess the influence of defects in GNRs on these thermal transport properties, especially focusing on Stone-Wales (SW) defects as a typical example. SW defects are pairs of pentagon-heptagon defects that are created by a 90° rotation of two carbon atoms with respect to the midpoint of the bond, as shown in Fig. 1. We used two complementary numerical approaches: (i) the nonequilibrium phonon Green's function (NEGF) technique[7–9] and (ii) the phonon-wave-packet scattering (PWS) technique.[10,11]

This Brief Report is organized as follows. In Sec. II, we introduce the Hamiltonian for lattice vibration of ZGNRs, and briefly explain the NEGF and the PWS techniques. In Sec. III, we show that the thermal current flows ballistically along the edges of the ZGNRs in the low-energy region, while the high-energy phonons are strongly scattered. We find that a noticeable circulating thermal current appears in the heptagonal rings of the SW defect around specific energies at which the phonon transmission probability is reduced to zero. Section IV is devoted to summary.

II. MODEL AND METHODS

The system considered in this Brief Report is an infinitely long GNR with a single SW defect. It is divided into three regions: left, central, and right regions (Fig. 1). The semi-infinite left and right regions have perfect periodicity along the ribbon axis and are assumed to be in thermal equilibrium. Their temperatures are higher and lower than the central region, respectively, therefore the thermal current flows from the left to the right. At a low temperature of several tens of Kelvins, the thermal current in ZGNRs is dominantly carried by phonons, not by electrons, because they have a band gap on the order of 0.1 eV in a typical ZGNR.[12] Since phonons in GNRs show no hybridization between the in-plane and the out-of-plane vibrational modes, the Hamiltonian between the in-plane and the out-of-plane modes can be completely decomposed. We will mainly consider thermal transport related to the out-of-plane modes in this Brief Report. Within the harmonic approximation, the Hamiltonian for the out-of-plane modes in the GNRs is described as

$$H = \sum_{i \in \mathrm{sys}} \left[\frac{p_i^2(t)}{2M} + \sum_{j>i} \frac{k_{ij}}{2} (z_i(t) - z_j(t))^2 \right]. \quad (1)$$

Here, $z_i(t)$ is the out-of-plane displacement from the equilibrium of the ith carbon atom of mass M along the z direction, $p_i(t)$ is the momentum of the ith atom, and k_{ij} is the spring constant between the ith atom and the jth atom. The spring constants between nearest-neighbor carbon atoms and those between the next-nearest-neighbor carbon atoms are estimated to be $k=5.3$ eV/Å^2 and $k'=\alpha k$ with $\alpha=0.05$, respectively, from Brenner's empirical potential.[13]

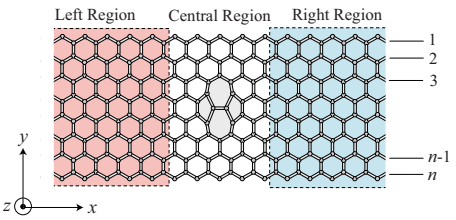

FIG. 1. (Color online) Schematic of a ZGNR with $n=8$ width with a SW defect.

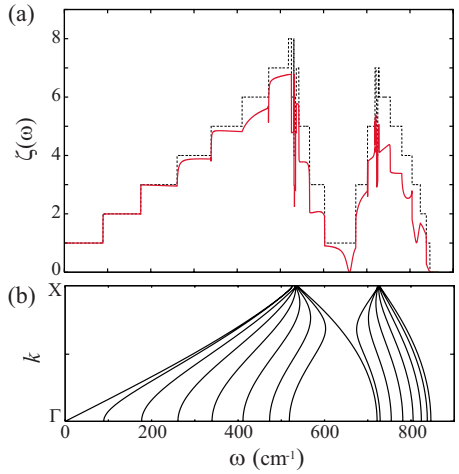

FIG. 2. (Color online) The phonon transmission function for out-of-plane phonons with 8-ZGNR with the SW defect (solid curve) and without a defect (dashed curve). (b) The phonon dispersion relations for the left lead of an 8-ZGNR junction shown in Fig. 1.

According to the Landauer theory of phonon thermal transport,[14] the thermal conductance can be expressed as

$$\kappa(T) = \int_0^\infty \frac{d\omega}{2\pi}\hbar\omega\left[\frac{\partial f(\omega,T)}{\partial T}\right]\zeta(\omega), \qquad (2)$$

when the temperature difference between the hot and cold heat reservoirs is small. Here, T is the averaged temperature between the two heat reservoirs, f is the Bose-Einstein distribution function, and $\zeta(\omega)$ is the phonon transmission function. If the phonon transmission is perfect for all acoustic modes, the thermal conductance at low temperatures is quantized as the universal value, $\kappa_0 = \pi^2 k_B^2 T/3h$, per acoustic phonon mode.[15]

It turns out from Eq. (2) that the phonon transmission function $\zeta(\omega)$ determines the thermal transport properties of the system. Recently, several methods for calculating $\zeta(\omega)$ for nanoscale objects have been developed. We used the NEGF method and the PWS method, which are detailed in Refs. 7–9 and Refs. 10 and 11, respectively.

III. RESULTS AND DISCUSSIONS

Figure 2(a) shows $\zeta(\omega)$ for a ZGNR with width $n=8$ (8-ZGNR) with and without an SW defect, calculated using the NEGF approach. n is the number of zigzag chains forming the ribbon (see Fig. 1). The dashed curve shows the evolution of $\zeta(\omega)$ with the phonon energy for a pristine 8-ZGNR without defects and exhibits a stepwise structure that gives the number of out-of-plane phonon branches, as depicted in Fig. 2(b). In this case, the propagating phonons in each branch are not scattered and they are transmitted perfectly through the ribbon. The solid curve in Fig. 2(a) represents $\zeta(\omega)$ for the defective 8-ZGNR, with the SW defect. In this case, the transmission function (solid curve) differs noticeably from that of the pristine 8-ZGNR, especially in the high-frequency region above $\omega \sim 250$ cm^{-1}. In particular, we observe a zero-transmission dip $[\zeta(\omega)=0]$ at $\omega=660$ cm^{-1} for which no phonon contributes to the thermal current. We discuss this unique phenomenon in detail later in this Brief Report.

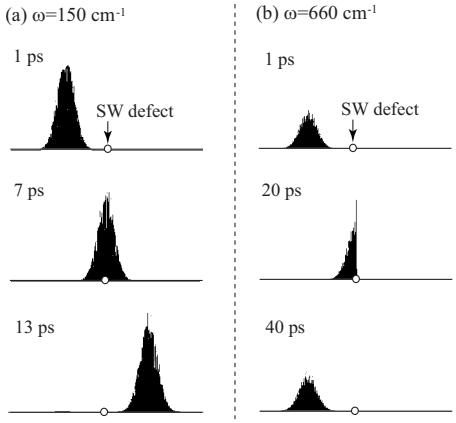

FIG. 3. Snapshots of time evolution of kinetic energy of a wave packet with (a) $\omega=150$ cm^{-1} on the acoustic phonon band and (b) $\omega=660$ cm^{-1}.

In contrast to the high-frequency region, the solid curve coincides with the dashed curve in the low-frequency region, below $\omega \sim 250$ cm^{-1}. Perfect transmission in this region occurs because the wavelengths of phonons are much longer than the size of the SW defect. Thus, the thermal conductance for GNRs is found to be quantized as the universal value at low temperature from Eq. (2) even in the presence of the SW defect. Similarly, in the case of the in-plane phonon modes, perfect phonon transmission is observed in the low-energy region.

The PWS simulations allow us to visually capture the previously described perfect transmission below $\omega \sim 250$ cm^{-1} and the perfect reflection at $\omega=660$ cm^{-1}. Figure 3 shows snapshots of the time evolution of the kinetic energy of a phonon wave packet with (a) $\omega=150$ cm^{-1} (on the acoustic phonon branch) and (b) $\omega=660$ cm^{-1} in the 8-ZGNR with the SW defect. The wave packet shot from the left lead has the shape of a Gaussian function with a broadening width of $\sigma=\frac{\pi}{200L}$ Å^{-1} in k space ($L=2.49$ Å is the length of the unit cell in the left and/or right region of the 8-ZGNR). As shown in Fig. 3(a), the acoustic phonon wave packet with $\omega=150$ cm^{-1} propagates through the SW defect without reflection. Similarly, we also found that the optical phonon wave packet with $\omega=150$ cm^{-1}, which is another branch lying at $\omega=150$ cm^{-1}, transmits perfectly through the 8-ZGNR (not shown in Fig. 3). On the other hand, as illustrated in Fig. 3(b), the wave packet is perfectly reflected by the SW defect at $\omega=660$ cm^{-1}. These PWS results are in perfect agreement with the NEGF results discussed earlier.

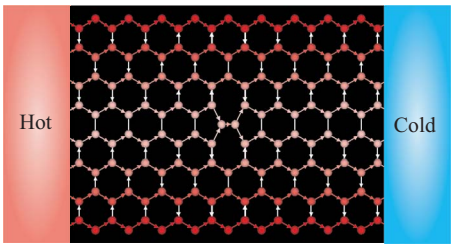

FIG. 4. (Color online) The phonon number and the bond thermal current in the scattering region of 8-ZGNR at $\omega=150$ cm^{-1}. The thermal current is dominantly flowing through the ribbon edges.

We attempted to clarify the phonon scattering dynamics around the SW defect from a microscopic point of view by calculating the spatial distributions of the phonon numbers and by analyzing the thermal current near the SW defect. The phonon number on the jth atom is expressed as

$$\rho_j(\omega) = i\hbar G_{jj}^{<}(\omega) \tag{3}$$

and the bond thermal current flowing from the ith atom to the jth atom is described by

$$J_{ij}(\omega) \propto \hbar\omega \,\mathrm{Re}[k_{ji}G_{ij}^{<}(\omega) - k_{ij}G_{ji}^{>}(\omega)] \tag{4}$$

in terms of the lesser and greater Green' functions. Figure 4 shows $J_{ij}(\omega)$ and $\rho_j(\omega)$ around the SW defect at $\omega=150$ cm^{-1}. The colors of the arrows and atoms represent the magnitudes of $J_{ij}(\omega)$ and $\rho_j(\omega)$, respectively. As shown in Fig. 4, the thermal current at $\omega=150$ cm^{-1} mainly flows through the ribbon edges; therefore, the phonons are not scattered even in the presence of the SW defect. The thermal current shown in Fig. 4 is carried by the acoustic and the lowest optical phonon modes near Γ point. The lowest optical phonons near Γ point are strongly localized around the edges, while the acoustic phonons near Γ point are delocalized over the ribbon. Therefore, the edge-flowing component of the thermal current in Fig. 4 originates from the lowest optical phonons. In other words, the edge-flowing thermal current does not appear in the low temperature region where the lowest optical phonons are not excited. This is a remarkable difference between electronic and phononic states.

On the other hand, the phonons at $\omega=660$ cm^{-1} do not contribute to the thermal current (i.e., $J_{ij}=0$) and there is perfect backscattering by the SW defect. Figures 5(a) and 5(b) show $J_{ij}(\omega)$ and $\rho_j(\omega)$ around the SW defect at $\omega=659$ cm^{-1} (immediately below the zero-transmission dip at $\omega=660$ cm^{-1}) and at $\omega=661$ cm^{-1} (immediately above the dip), where the net thermal current passing from the left to the right leads is rather small. Interestingly, the clockwise and counterclockwise circulating thermal currents, respectively, flow along the lower and upper heptagonal rings of the SW defect at $\omega=659$ cm^{-1} [Fig. 5(a)] and vice versa at $\omega=661$ cm^{-1} [Fig. 5(b)], although the net thermal current does not change its direction. These results are also confirmed by the PWS method.

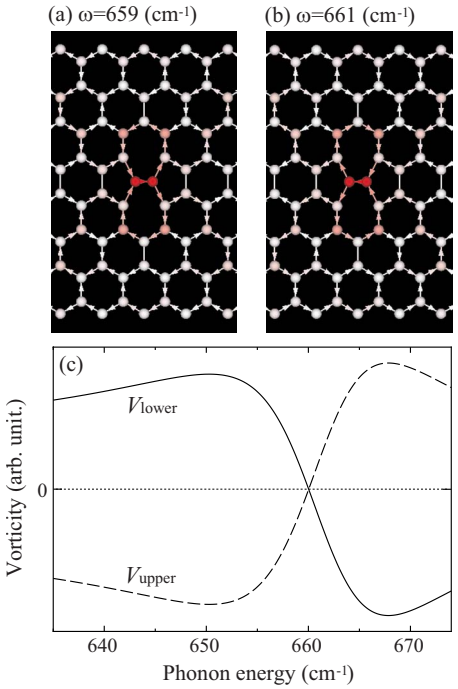

FIG. 5. (Color online) The phonon number and the bond thermal current around the SW defect at (a) $\omega=659$ cm^{-1} (immediately below the zero-transmission dip) and (b) at $\omega=661$ cm^{-1} (immediately above the dip). (c) The local vorticity with respect to the bond thermal current flowing on the upper (dashed curve) and lower (solid curve) heptagonal rings of the SW defect.

In order to discuss the features of the circulating thermal currents in more detail, we introduce the local *vorticity* that is defined as the clockwise sum of the bond thermal current of the upper and lower heptagonal rings as follows:

$$V_p(\omega) = \sum_{\langle ij\rangle=1}^{7} J_{ij}^{(p)}(\omega) \quad (p = \text{upper or lower}), \tag{5}$$

where $J_{ij}^{(p)}$ denotes the thermal current on the nearest-neighbor $\langle ij\rangle$ bond of the p=upper and/or lower heptagonal ring. Figure 5(c) shows V_{upper} (dashed curve) and V_{lower} (solid curve). The solid (dashed) curve changes its sign from positive (negative) to negative (positive) when crossing the zero-transmission dip of $\omega=660$ cm^{-1}, which occurs as a result of the circulating thermal currents reversing their directions at $\omega=660$ cm^{-1}. Also, the circulating thermal currents can be observed only near the zero-transmission dip at $\omega=660$ cm^{-1}. From these results, zero transmission is caused by the superposition of two time-reversal symmetric states with opposite thermal flows, as in Figs. 5(a) and 5(b). Similar phenomena have been observed for electronic transport in GNRs with defects.[3,4]

IV. CONCLUSION

In conclusion, we have numerically studied thermal transport through GNRs with and without SW defects using the NEGF and PWS methods. We found two unique thermal

transport phenomena occurring at different energy regions; an edge-localized thermal current at low energies and a circulating thermal current along the heptagonal rings of the SW defect around $\omega=660$ cm^{-1}. By calculating the local vorticity, we can understand the mechanism for the appearance of the circulating thermal current in terms of the interference of two states of opposite parity. Further theoretical studies are necessary to fully understand the underlying physics of this behavior.

ACKNOWLEDGMENTS

This study was supported in part by Ministry of Education, Culture, Sports, Science and Technology of Japan (MEXT) through Grants-in-Aid (No. 30408695 and No. 19540411). Some of the numerical calculations were performed on the Hitachi SR11000s at the ISSP at the University of Tokyo.

[1] L. G. Cancado, M. A. Pimenta, B. R. A. Neves, G. Medeiros-Ribeiro, T. Enoki, Y. Kobayashi, K. Takai, K. I. Fukui, M. S. Dresselhaus, R. Saito, and A. Jorio, Phys. Rev. Lett. **93**, 047403 (2004).

[2] M. Fujita, K. Wakabayashi, K. Nakada, and K. Kusakabe, J. Phys. Soc. Jpn. **65**, 1920 (1996).

[3] K. Wakabayashi and M. Sigrist, Phys. Rev. Lett. **84**, 3390 (2000).

[4] K. Wakabayashi, Phys. Rev. B **64**, 125428 (2001).

[5] S. Soma, T. Yamamoto, and K. Watanabe, e-J. Surf. Sci. Nanotechnol. **4**, 78 (2006).

[6] T. Yamamoto, K. Watanabe, and K. Mii, Phys. Rev. B **70**, 245402 (2004).

[7] T. Yamamoto and K. Watanabe, Phys. Rev. Lett. **96**, 255503 (2006).

[8] N. Mingo, Phys. Rev. B **74**, 125402 (2006).

[9] J.-S. Wang, J. Wang, and N. Zeng, Phys. Rev. B **74**, 033408 (2006).

[10] P. K. Schelling, S. R. Phillpot, and P. Keblinski, Appl. Phys. Lett. **80**, 2484 (2002).

[11] N. Kondo, T. Yamamoto, and K. Watanabe, Jpn. J. Appl. Phys., Part 2 **45**, L963 (2006).

[12] Y.-W. Son, M. L. Cohen, and S. G. Louie, Phys. Rev. Lett. **97**, 216803 (2006).

[13] D. W. Brenner, Phys. Rev. B **42**, 9458 (1990).

[14] L. G. C. Rego and G. Kirczenow, Phys. Rev. Lett. **81**, 232 (1998).

[15] T. Yamamoto, S. Watanabe, and K. Watanabe, Phys. Rev. Lett. **92**, 075502 (2004).